A Grand Canonical DFT Investigation of the CO2RR and HER Reaction Mechanisms on $MoTe_2$ Edges

Pernille D. Pedersen,[†] Marko M. Melander,[‡] Thomas Bligaard,[†] Tejs Vegge,[†] Karoliina Honkala,[*,‡] and Heine A. Hansen[*,†]

†*Department of Energy Conversion and Storage, Technical University of Denmark, Anker Engelunds Vej 1, 2800 Kgs. Lyngby, Denmark*

‡*Department of Chemistry, Nanoscience Center, University of Jyväskylä, P.O. Box 35, FI-40014 Jyväskylä, Finland*

E-mail: karoliina.honkala@jyu.fi; heih@dtu.dk

Abstract

$MoTe_2$ has experimentally and theoretically been identified as a promising cathode candidate for electrocatalytic CO_2 reduction (CO2RR). A full understanding of its reactivity requires special consideration of the reaction kinetics, but this is challenging due to the varying electrode potential in the canonical DFT, which calls for grand canonical, constant potential methods. Here, the full reaction pathways for CO2RR to CO and the competing Hydrogen Evolution Reaction (HER) are investigated on a $MoTe_2$ edge in an alkaline medium using a Grand Canonical Ensemble DFT approach with hybrid solvent model to understand the explicit effect of the applied potential. Our results show that the barrier of the first CO2RR step, the CO_2 adsorption, is lower than the first HER step, the Volmer step, which implies that CO2RR is favored. We also find that at more negative potentials the first CO2RR steps become more favorable, whereas CO desorption becomes less favorable, indicating that further CO reduction is expected instead of CO desorption. However, the potential dependence of the Volmer step depends more strongly on potential than CO_2 adsorption, making HER more favorable at more negative potentials. Overall, our study identifies edge-rich $MoTe_2$ nanoribbons as possible catalysts for alkaline CO2RR.

Introduction

The electrocatalytic reduction of CO_2 (CO2RR) is a promising pathway towards closing the anthropogenic carbon cycle.[1,2] In this process, CO_2 gas captured from point sources or directly from ambient air (DAC) is converted into various carbon products, which can be used as both fuels or chemicals. Among the most common products are CO and formate/ formic acid, while only a few proposed catalysts have been observed forming further reduced products, such as alkanes or alcohols.[3–5] While copper is the only "beyond CO" producing transition metal, it is associated with high overpotentials and poor selectivity.[6–9] Recently, transition metal dichalcogenides (MX_2, X=S, Se, Te) have attracted significant interest for

electrocatalysis.[10–15] In particular, MoS_2 has been widely studied for various applications of electrocatalysis and energy materials.[14–17]

The transition metal dichalcogenides (TMDC) have also attracted growing attention for CO2RR.[18–22] In our recent study, we showed that transition metal tellurides exhibit promising thermodynamic properties for CO2RR, as they adsorb H weakly and CO strongly compared to sulfides and selenides.[23] This behaviour is expected to lead to the formation of beyond-CO products[24] in agreement with an experimental study identifying CH_4 as a major product of $MoTe_2$ nanoflakes in an ionic liquid.[25] Interestingly, in the same study, some CO2RR activity was measured even in an aqueous electrolyte, further indicating of the suppression of the competing HER. In particular, the edge sites have been proposed to be important for the TDMC catalysts and they can, for example, enhance electronic conductivity. In the case of $MoTe_2$, its most stable phase, the 2H-phase, is a semiconductor in bulk but metallic edge states arise upon formation of nanostructures.[26,27] The pristine 2H-$MoTe_2$ edges are assumed to be the active sites for catalysis[28–30] while defects are required to activate the basal plane of 2H-$MoTe_2$[31,32] and the high acidic HER activity of $MoTe_2$ is associated to the basal plane anion vacancies.[33] Based on these findings, we expect that pristine 2H-$MoTe_2$ edges will exhibit high CO2RR activity and suppress HER in alkaline electrolytes.

To test the validity of this proposal, the reaction kinetics of CO2RR and the competing HER needs to be addressed. However, modeling reactions at the electrochemical solid-liquid interface is not straightforward.[34–37] During an electrochemical reaction, electrons are transferred to or from the working electrode, kept at constant potential. While in an experimental setup, this is achieved via an external circuit, in common canonical simulations, the number of electrons is fixed and the Fermi level of the electrode, *i.e.* the electrode potential, fluctuates over the course of an electrochemical reaction.[38] Common post-processing approaches such as the Computational Hydrogen Electrode (CHE)[39] have proven successful in describing the potential dependence of reaction thermodynamics of proton coupled electron

transfer reactions. However, it cannot be used when charge is directly transferred during the simulation, *e.g.* in reaction barrier calculations.[39] Furthermore, charge transfer reactions not involving a simultaneous proton transfer cannot be described with CHE. The electrode potential effects can be explicitly described with Grand Canonical Ensemble (GCE) based methods, such as GCE-DFT, where the electrochemical potential of an electron, *i.e.*, the electrode potential, rather than the number of electrons is kept fixed.[38,40] GCE-DFT -based approaches have previously provided detailed descriptions of various electrochemical reaction pathways, such as the NRR/ HER on Ru-N_4,[41] Au-Catalyzed Glycerol Electro-oxidation,[42] and the HER at MoS_2[43] and $MoTe_2$ basal planes.[33] Also, the CO2RR has been the subject of GCE-DFT investigations. On the Cu(100) surface, a potential dependence of the C-C bond formation mechanism was demonstrated considering reaction barriers and thermodynamics,[44] while a later study identified the hydrogenation of CO_2 to be the rate limiting step of the CO2RR on Ag(110) using a multiscale modelling approach including reaction kinetics.[45] The CO2RR/ HER competition has also been investigated and significantly different potential dependencies for reaction energies of CO2RR and HER elementary steps were reported on various (111) transition metal surfaces[46] but kinetic considerations were excluded. Most recently, the pH and potential dependence of the rate limiting step in the formation of multi-carbon species on Cu was investigated.[47]

In this paper, the alkaline CO2RR and HER reactions at a $MoTe_2$ edge is investigated considering reaction thermodynamics and kinetics as a function of the electrode potential. Specifically, the potential dependence of relevant reaction barriers of the CO2RR and competing HER reactions at $MoTe_2$ edges are evaluated through GCE-DFT calculations. We show that CO2RR is kinetically favored over HER, explaining the CO2RR activity observed in an aqueous electrolyte.[25] We also find that the barrier for a CO desorption step is increased at more reducing potentials, indicating that beyond-CO reduction could become increasingly favorable compared to CO desorption. Our findings identify edge-rich $MoTe_2$ as an active and selective catalyst towards CO2RR in alkaline electrolytes.

Computational methods

All DFT calculation were performed in a projector augmented wave (PAW) formalism as implemented GPAW 21.6.0[48,49] integrated with the Atomic Simulation Environment (ASE).[50] Most calculations were performed in Finite Difference (FD) mode using a grid spacing of 0.16 Å but the minima hopping calculations (see below) were carried out in LCAO mode with a DZP basis set in order to limit the computational cost. The employed exchange-correlation functional is in all cases the the BEEF-vdW functional,[51] which includes van der Waals effects for accurate thermodynamics of adsorption reactions. The electrons are smeared using a Fermi-Dirac smearing with a width of 0.05 eV. Atomic positions are relaxed until all residual forces are below 0.06 eV/ Å. Periodic boundary conditions are applied in the x and y directions with an employed (5x1x1) k point mesh), while an added empty space of 8 and 10 Å respectively is added to each side of the structure in the y and z directions respectively, to create the nanoribbon with edges. The configuration of the edge is motivated by our recent findings and will be addressed in detail below. A dielectric-dependent dipole correction[52] is applied in the xy direction to allow for a potential difference across the system.

The electrochemical solid-liquid interface is modelled by an implicit/explicit hybrid solvent approach combining the Simple Continuum Model based on Volumetric Data (SCMVD) dielectric continuum model with 4 explicit water molecules.[53] The implicit solvent is defined within a box-shaped region above the $MoTe_2$ edge in the z-direction ranging from 1 Å above the outermost atom in the cell and 1 Å below the top of the cell. The vdW-radii are adapted from the GPAW database, except for Mo, for which a value of a value of 2.1 Å is employed.[54] The Minima Hopping method as implemented in ASE is used to optimize the location and orientation of the explicit water molecules.[55] For the CO2RR the water layer is optimized for CO_2 adsorbed at the edge, whereas for the HER the water layer is optimized for the pristine surface. In each case four water molecules are included in the water layer. Each initial and final state for the different reaction steps is then constructed using the obtained minimum energy water layer structure as the starting point. The proton donor for the proton coupled

electron transfer reactions is the explicit water molecule closest to the reaction site. In these reactions, the final state involves an OH^- ion, which subsequent reaction step is replaced by a H_2O molecule and the original water layer is regained. Initial and final states are obtained by relaxing the three outermost rows of edge atoms (Te, Mo, Te), the adsorbed species and all explicit water molecules, while keeping the additional surface atoms fixed.

Grand canonical free energies at fixed potentials are obtained using the Solvated Jellium Model (SJM) method as implemented in GPAW.[52] In this approach, a homogeneous counter charge (a jellium slab) positioned within the implicit solvent region is added to keep the system charge neutral, while the number of electrons in the cell is iteratively adjusted until the target potential (Φ_e) is reached within a tolerance threshold of 0.025 V. The implicit solvent and neutralizing jellium counter charge screen the surface charge and high electric field originating from the charge surface. In SJM the electrode potential is defined as the Fermi level (E_f) referenced to the electrostatic potential deep in the implicit solvent (Φ_w), where no electric field is present:

$$\Phi_e = \Phi_w - E_f \tag{1}$$

The experimentally determined relation between Φ_e and the potential against the Standard Hydrogen Electrode (U_{SHE}) is given by:[56]

$$U_{SHE} = \Phi_e - 4.44V \tag{2}$$

For better comparison with experiments, the potentials are converted to the Reversible Hydrogen Electrode (RHE) scale using:

$$U_{RHE} = U_{SHE} + k_B T \cdot pH \cdot ln(10) \tag{3}$$

Where k_B is the Boltzmann constant and T is the absolute temperature. The energies used

in this study are the grand free energies, Ω, defined as:

$$\Omega = E_{tot} + \Phi_e N_e \tag{4}$$

Here, E_{tot} is the DFT calculated energy and N_e is the number of excess electrons. For molecular references, the gas phase Gibbs free energy including zero-point energy and entropy is employed. In the special case of $H^+ + e^-$, the energy is calculated by:

$$G_{H^+ + e^-} = 0.5 G_{H_2} - eU_{RHE} \tag{5}$$

where G_{H_2} is the Gibbs free energy of a dihydrogen molecule. The potential is corrected for by the -eU_{RHE} term, where e is the number of electrons, and U_{RHE} is the applied potential. Finally, reaction grand free energies are calculated by:

$$\Delta\Omega = \Omega_{products(*)} + G_{products(g)} - \Omega_{reactants(*)} - G_{reactants(g)} \tag{6}$$

where * denotes surfaces and adsorbed species and g denotes gas phase species.

Nudged Elastic Band (NEB) calculations as implemented in ASE[57,58] are performed to obtain the grand free energy barriers. In some cases the bond length between the reacting species in the solvent and the Mo reaction site is additionally constrained to ensure a shorter NEB path, while preventing recombination of reactants. In this case, an intermediate image from a previously non-converged NEB run is chosen as the initial guess for relaxation. Linear interpolation between initial and final state is employed to construct the initial guess for the NEB path. Finally, the climbing image method is employed to get a better description of the saddle point.[59] The potential is fixed during NEB and CI-NEB optimizations. The atomic charges are computed using the Bader charge analysis scheme.[60–63] The charge difference

between an atom in the final and initial state is then calculated as

$$\Delta q = q_f - q_i \tag{7}$$

where q is the Bader charge of the atom in question, and i and f indicate the initial and final states, respectively.

Results and discussion

A single layer of the 2H phase of $MoTe_2$ consists of a hexagonal layer of Mo atoms sandwiched between two layers of Te atoms stacked in an eclipsed configuration, so that each Mo atoms upholds a trigonal prismatic lattice coordinating to six Te atoms. Cutting the 3D sheet stoichiometrically in the so-called "zig-zag" direction creates a nanoribbon with two edges terminated by Te atoms (X edge) and Mo atoms (M edge), respectively. However, under experimental conditions, reorganization of the edge configuration is likely to occur.[64] In our previous study of the edge termination of TMDC nanoribbons using the CHE model, we found that OH terminated configurations of the X edge were favored under experimental conditions relevant for CO2RR, while also the adsorption energies for CO and H were more favorable at the M edge.[23] Hence, in this study, the Mo edge is selected as the reaction site.

Based on the previous results,[23] 5 different edge terminations were selected for investigations, here denoted as Te_2 (OH_2) with each Mo-Mo bridge site occupied by a Te (OH), Te_1 (OH_1) with every second gap occupied, and Te_1OH_1 with the terminating group alternating between Te and OH as shown in the insets of Figure 1. Furthermore, one termination in which CO_2 is adsorbed to the Mo site at the Te_1 terminated edge is considered, as it is expected to be the active site for CO2RR. All the terminations are initially considered without explicit solvent molecules.

The explicit potential and pH dependencies of the relative stabilities of different Mo edge

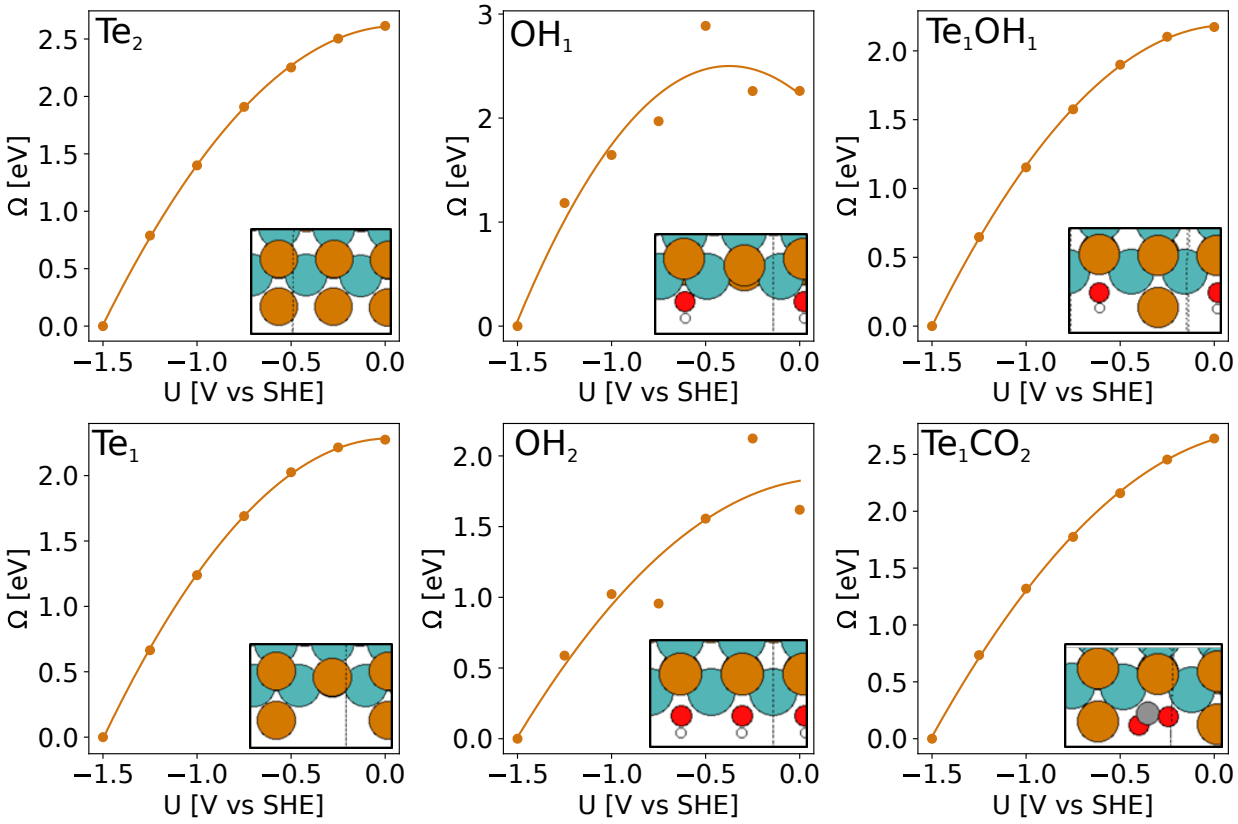

Figure 1: Variation of the Grand free energy, Ω, as a function of potential, U vs RHE, for six different terminations of the $MoTe_2$ M edge (shown as insets. Turquise=Mo, brown= Te, gray=C, red=O, white=H). The solid lines are second order fits to the data points, each corresponding to a GCE-DFT calculation at different potential. Here, a negative $\Delta\Omega$ value means that the reaction is thermodynamically favorable

terminations were investigated using the GCE-DFT. Figure 1 shows the grand free energies of six different terminations (shown as insets in Figure 1), each calculated at seven different potentials. The data has been fitted to second order polynomials in accordance with the expected potential dependence.[42,65,66] The data generally follow the expected trend, only for the OH terminated edges some deviation is observed. The grand free energy curvatures and maxima correspond to the capacitance and potential of zero charge (PZC), respectively. These are provided for each termination in SI (Table S1), and show that the PZC depends on the edge termination while the capacitance is fairly structure insensitive.

The obtained grand free energy fits are used to map the potential and pH-dependent

edge stabilities according to Equation 3 and the corresponding plots are given in Figure 2. The grand free energy as a function of potential at a fixed pH=7 is furthermore shown in Figure 3. The OH_2 termination is excluded from the analysis, as it is highly unstable in the entire region considered. Our results show that the relative stability of the terminations depends sensitively on potential with the lower Te coverage becoming more favorable with a decreasing electrode potential (top left) in agreement with our previous results.[23] The stabilities of the two OH terminated structures, OH_1 (top right) and Te_1OH_1 (bottom left), also increase at more negative potentials. For the Te terminated edges, the pH dependence is minimal, whereas the two OH terminations show a significant pH dependence; the OH_1 becomes relevant at low pH even for intermediate potentials. We attribute observed stabilization to the stronger dipole-field interactions resulting from inclusion of the polar OH-group and the large difference in the PZC for these to different surface terminations (see Table S1). The presence of a CO_2 adsorbate at the Te_1 termination does not notably alter the relative stability, indicating that adsorption of CO_2 is thermodynamically feasible and it does not significantly change the surface stability. In the earlier experimental study, the CO2RR activity was measured for potentials below -0.6 V at neutral conditions (ionic liquid/ 0.1 M $KHCO_3$).[25] At these conditions, we expect the Te_1 termination to dominate, hence it is chosen as the model system for the mechanistic analysis.

Potential-dependent reaction thermodynamics and kinetic barriers of CO2RR and HER

In order to calculate reaction barriers for the CO2RR and the competing HER, a layer of explicit water molecules was included above the most stable, Te_1 edge, see the Supplementary Figures S1-S3. The reactions and elementary steps considered are listed in Table 1 along with possible additional constraints employed in the optimization of the initial and final states for the NEB path. The optimized structures are shown in the SI Figures S2 and S3.

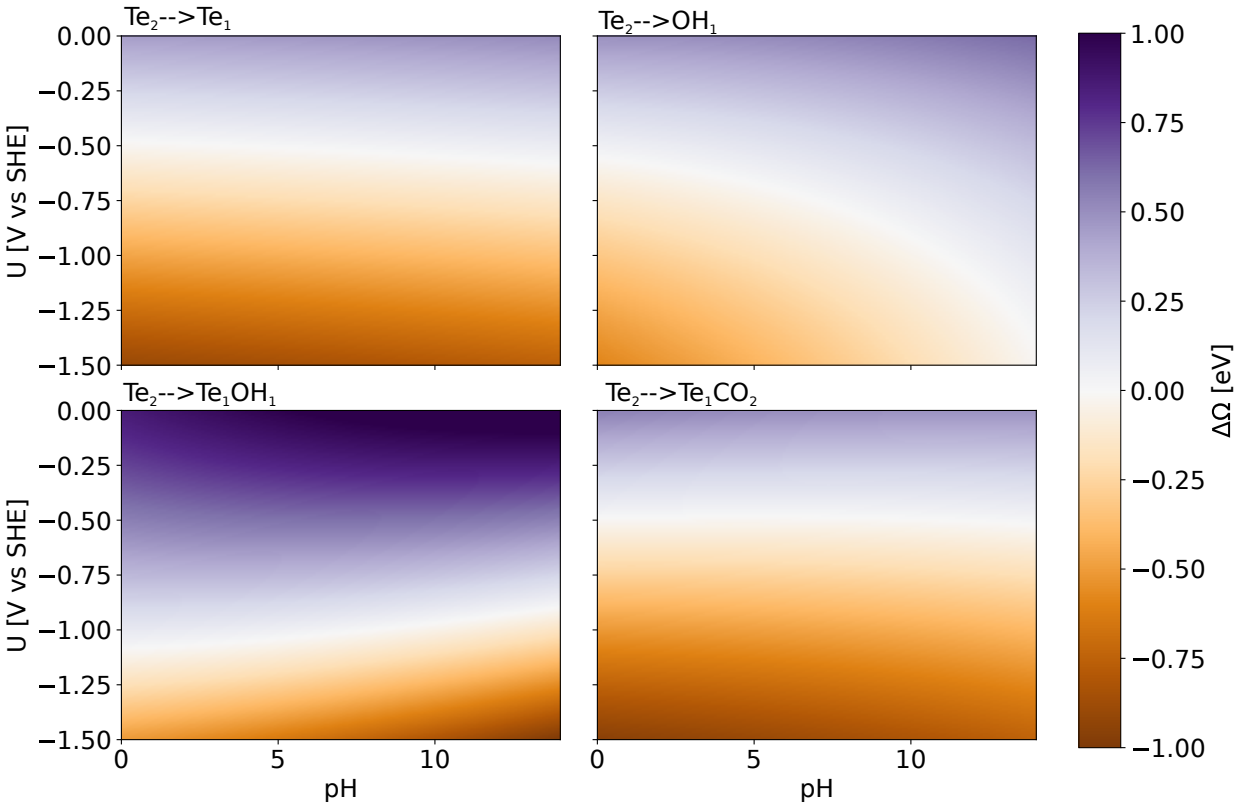

Figure 2: Heatmaps showing the relative stabilities of different edge termination relative to the Te_2 termination. $\Delta\Omega$ has been normalized to the number of electrons transferred.

The NEB paths calculated at three different potentials are given in Figure 4. For all four elementary steps, the charge of the system varies monotonously going from initial to final state over the transition state (SI Table S2), which is observed also for metallic systems.[52,67] Generally electrons are gained over the course of the reaction, except for CO desorption, where the number of electrons is decreased. CO_2 adsorption is found to be exergonic and sensitively depend on the electrode potential; this can only be captured with explicitly considering the electrode potential. The kinetic barrier is below 0.3 eV at all three potentials. The potential-dependency can be rationalized by the charge analysis given in Figure 5, which shows that the adsorbed CO_2 carries a substantial, ~ -0.8e charge. Table S2 displays that the total system gains 0.5 additional electrons during the adsorption to maintain fixed electrode potential. Projected density of states plots (PDOS) for CO_2 SI Figures S4 and 5 clearly show the σ donation from the adsorbate to the Mo d-states and the π backdonation

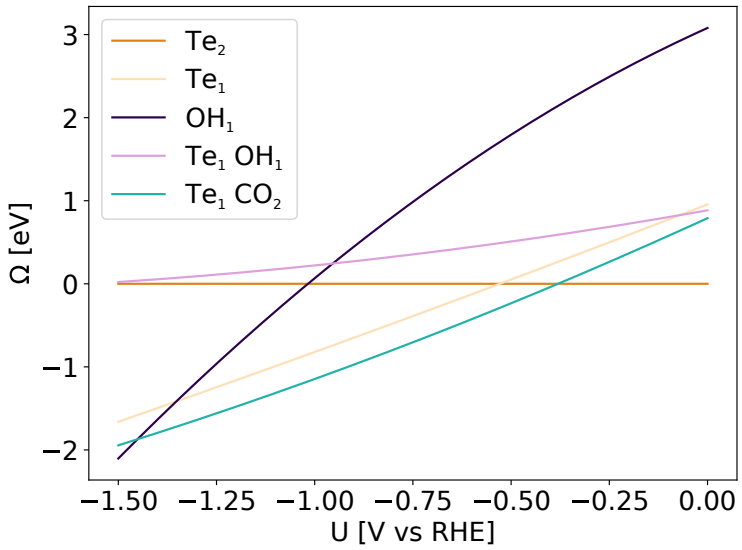

Figure 3: Grand free energy, $\Delta\Omega$, as a function of potential, V vs RHE calculated at pH=7.

from the d-states to the adsorbate π^* orbitals upon bonding. Together the charge and PDOS analyses demonstrate notable charge transfer from the surface to the orbitals of CO_2: the first CO2RR step corresponds to an electron transfer event.

While, the first H transfer leading to *COOH is thermodynamically uphill, the second H transfer leading to adsorbed *CO is exergonic. Note that the final states of the H transfer reactions involve an OH^- ion, which is subsequently replaced by a water molecule before the next elementary step achieving significant energy gain. The OH^- formed in the final state is not stabilized by an explicit cation, however, to keep the potential constant the number of excess electrons in the surface is increased (make the surface more negative) together with compensating the positively charged solvated jellium, as shown in Table S2. As expected, both barriers decrease at more negative potentials but the second H-transfer barrier is generally slightly lower than the first one (0.52 eV vs 0.68 eV at -1.23 V vs RHE).

The final CO2RR step, considered in this study, is the CO desorption, which is found to be thermodynamically unfavorable by more than 1.4 eV and associated with a correspondingly large forward reaction barrier. While this binding energy would lead to very slow CO desorption rates, it is possible that adsorbate-adsorbate repulsions on certain sites,

Table 1: The reactions steps considered. r_{Mo-C} is constrained in the initial state of the CO_2 adsorption step to minimize the length of the reaction path; necessary to converge the NEB calculation. For the Volmer steps, r_{Mo-O} is constrained in the final state to prevent recombination of H and OH.

Reaction	Step		Additional constraints
CO2RR	CO_2 adsorption	$CO_2 + * \rightarrow {}^*CO_2$	$r_{Mo\text{-}C}$ fixed in IS
	H transfer 1	$H_2O + {}^*CO_2 \rightarrow {}^*COOH + OH^-$	
	H transfer 2	$H_2O + {}^*COOH \rightarrow {}^*CO + OH^-$	
	CO desorption	${}^*CO \rightarrow CO + *$	
HER	Volmer 1	$* + H_2O \rightarrow {}^*H$	$r_{Mo\text{-}O}$ fixed in FS
	Heyrovsky	${}^*H + H_2O \rightarrow {}^*H_2$	
	Volmer 2	${}^*H + H_2O \rightarrow 2{}^*H$	$r_{Mo\text{-}O}$ fixed in FS
	Tafel	$2{}^*H \rightarrow {}^*H_2 + *$	
	H_2 desorption	${}^*H_2 \rightarrow H_2 + *$	

will weaken CO binding allowing it to desorb.[68] Interestingly, the barrier for CO desorption increases at more negative potentials indicating that CO formation becomes less favorable. This also implies that "beyond-CO" product formation may be enhanced for more negative potentials.[24] CO adsorption strength at the metal site is enhanced for TMDCs with decreasing polarity of the M-X bond and thereby increasing electron density on the metal.[23] A linear increase of the electron density would be likewise expected for decreasingly negative potentials, which possibly explains the increased barrier for CO desorption. This implies that π-backbonding is involved in the CO-bonding and the PDOS analysis, in SI Figure S5, clearly shows the σ donation from the CO adsorbate to the Mo d-states and the π backdonation from the d-states to the adsorbate π^* orbitals. The charge analysis for CO desorption in Figure 5 shows that charge transfer takes place from the surface to the adsorbate orbitals. While charge transfer is enhanced at more reducing potentials, it is more pronounced for CO than CO_2, which explains the stronger potential dependence of the CO desorption barrier (Figure 7). The precise number of water molecules and the structure of the explicit water layer can potentially influence the computed barrier values and thermodynamics. SI Figure S6 presents the NEB paths for the first H-transfer and the CO desorption steps using different water layers and demonstrates the impact of the water layer structure is minor. While

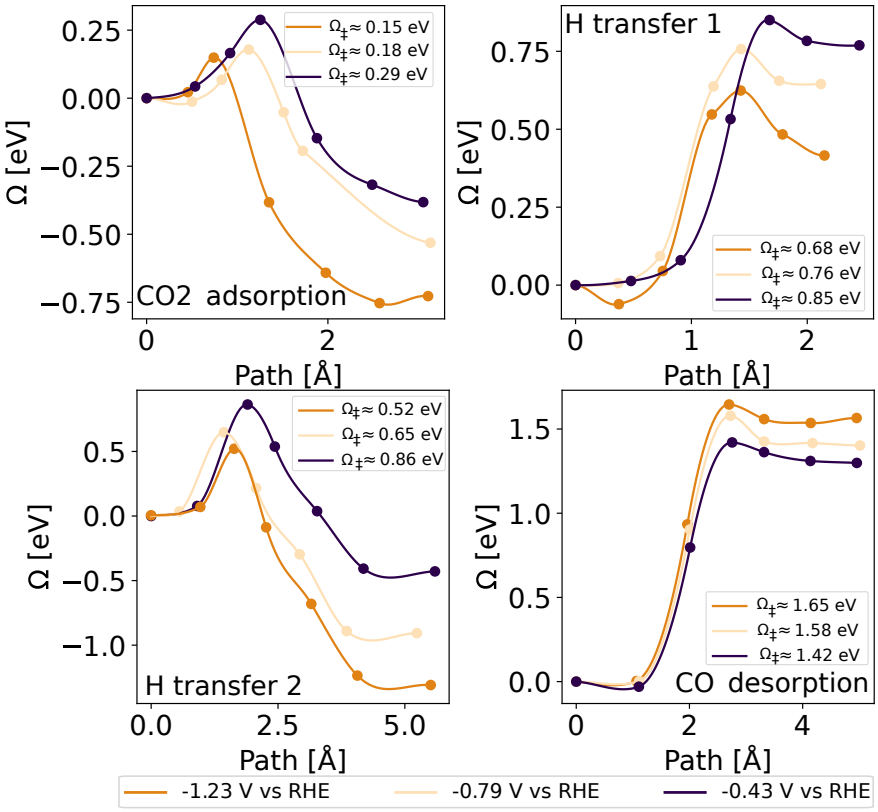

Figure 4: Free energy profiles for the CO2RR elementary steps calculated at different potentials. The value of the forward energy barriers, $\Omega_{\ddagger}$ is given for each potential in the legends.

different water structures can affect intermediates differently, the reaction energy of a full catalytic cycle will be independent of the water structure.

The HER can proceed either via the Volmer-Heyrovsky or the Volmer-Tafel mechanism. In both cases, the reaction starts with the Volmer step, where H adsorbs from the solvent, followed either by the Heyrovsky step (Table 1) or an additional Volmer step and a subsequent Tafel step (Table 1) and finally H_2 desorption. The NEB paths calculated at three potentials are shown in Figure 6). For all the elementary steps the charge monotonously increases (Volmer 1, Volmer 2 and Heyrovsky) or decreases (H_2 desorption) over the course of the reaction (shown in SI Table S2). The only exception being the Tafel reaction, for which a slight non-linearity is observed; the charge is decreased from the initial to the transition state and increased from the transition to the final state. This indicates higher sensitivity of the

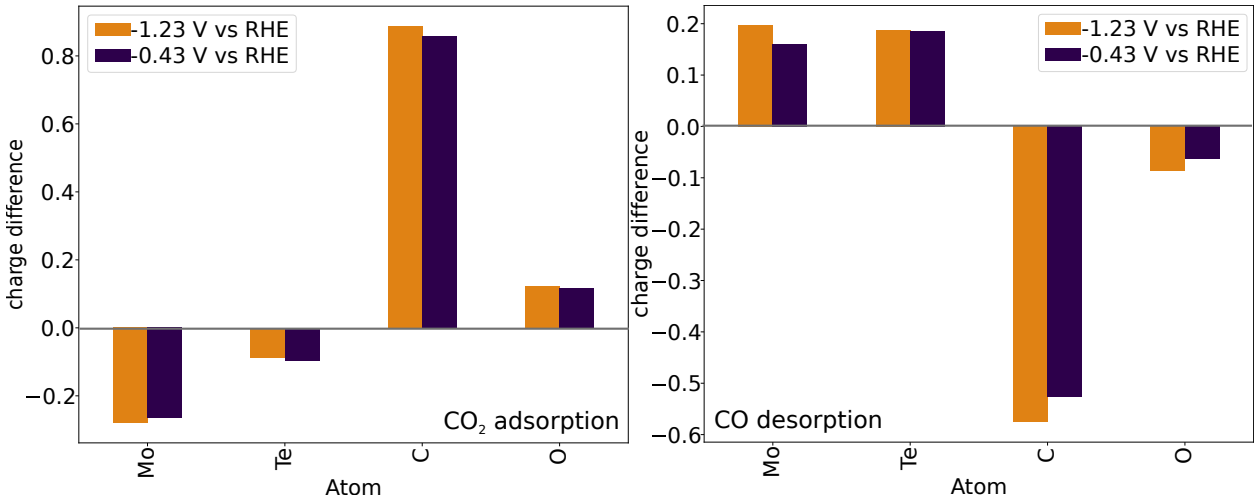

Figure 5: Δq calculated by the Bader charge analysis scheme for C and O atoms in CO_2 and CO, the Mo atom in the adsorption site, and the neighboring Te atom. CO_2 adsorption (left) and CO desorption (right). The positive charge difference correspond to charge tranfered to the atom over the course of the reaction

reaction barrier than the reaction energy to the potential.[41] The change in charge through the reaction is minor for the Tafel step. The reaction barriers for the two Volmer and one Heyrovsky steps are rather high (1.07 eV, 1.20 eV and 0.84 eV at -1.23 V vs RHE) and all three reactions are also thermodynamically unfavorable. It should, however, be noted that the reformation of the charge-neutral water layer upon OH^- ion replacement is associated with large energy gain, so that the reactions actually become thermodynamically downhill.

Comparing the barriers for the Heyrovsky step and the second Volmer step (the second step in the Volmer-Heyrovsky and Volmer-Tafel mechanism respectively) shown in Figure 6, the Volmer-Heyrovsky mechanism is expected to be the relevant HER mechanism at the electrode potentials considered here. The reaction barriers of the Volmer1, Volmer2, and Heyrovsky steps decrease as more reducing potentials are applied. The final elementary step of the HER pathway is the desorption of H_2. In the preferred adsorption geometry, the H_2 molecule adsorbs flat on the Mo-site with both H atoms bonding to the Mo atom and the H-H bond being elongated. Two different configurations, shown in SI Figure S3, are found with bond lengths of 1.86 Å ($^*H_2^a$) and 0.82 Å ($^*H_2^b$) with $^*H_2^a$ being 0.26 eV lower in energy than $^*H_2^b$. The desorption barrier is 0.30 eV larger for $^*H_2^a$ than for $^*H_2^b$. $^*H_2^a$ is found to be

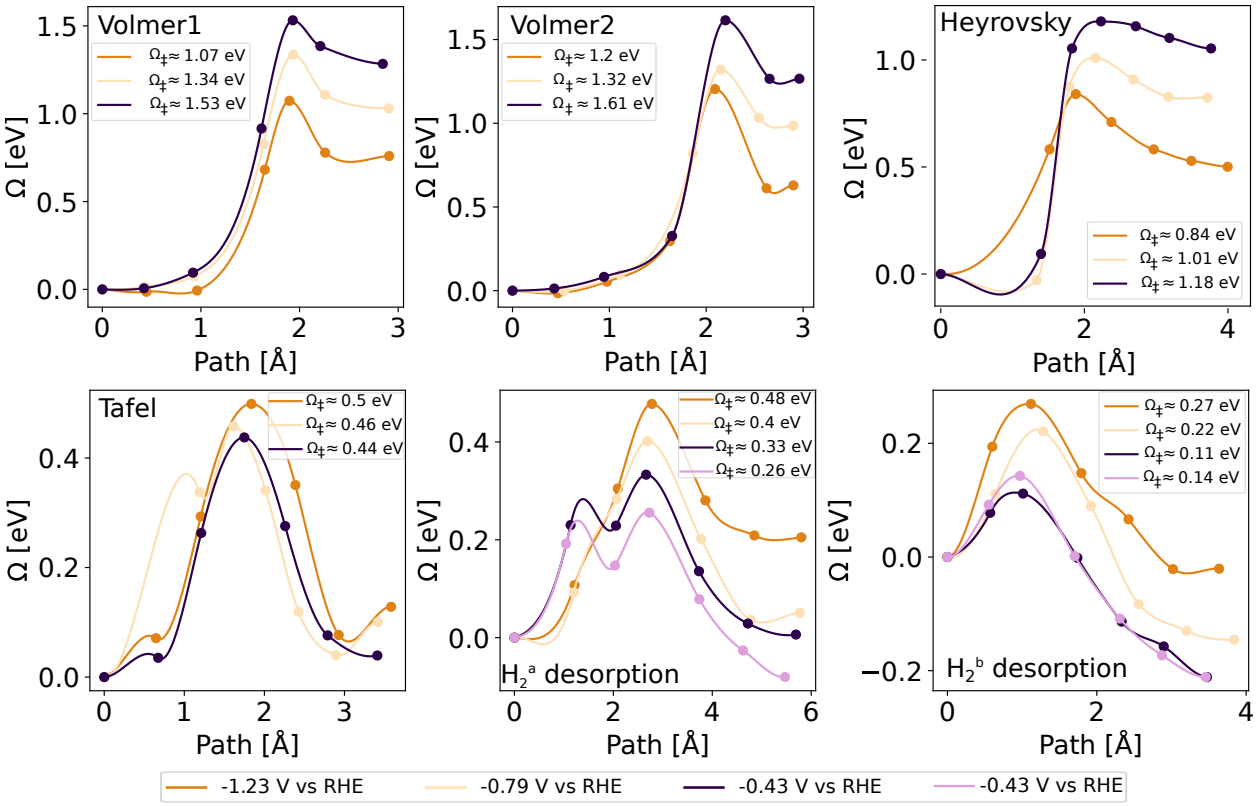

Figure 6: Free energy profiles for the HER elementary steps calculated at different potentials. The value of the forward energy barriers, $\Omega_{\ddagger}$ is given for each potential in the legends.

the preferred final state of the Tafel step. The Heyrovsky mechanism is conversely found to proceed via $^*H_2^b$ as the barrier to $^*H_2^a$ is found to be larger. The desorption of H_2^a is found to involve two reaction steps; $^*H_2^a \rightarrow {}^*H_2^b$ and $^*H_2^b \rightarrow H_2(g) + ^*$. At highly reducing potentials, the first step is found to be negligible, whereas it becomes increasingly important at less negative potentials (visible as the shoulder in the NEB path in Figure 6 bottom center, which arises for low potentials). The barrier for the direct desorption of the energetically less favorable H_2b is lowered by approximately 0.2 eV compared to that of H_2^a.

Figure 7 summarizes the grand free energy barriers of the CO2RR and HER elementary steps for different potentials. Interestingly, the potential-dependency for the first Volmer step is more pronounced than for the CO_2 adsorption, and thus HER becomes relatively kinetically more favorable at more negative potentials. However, the barrier for the first

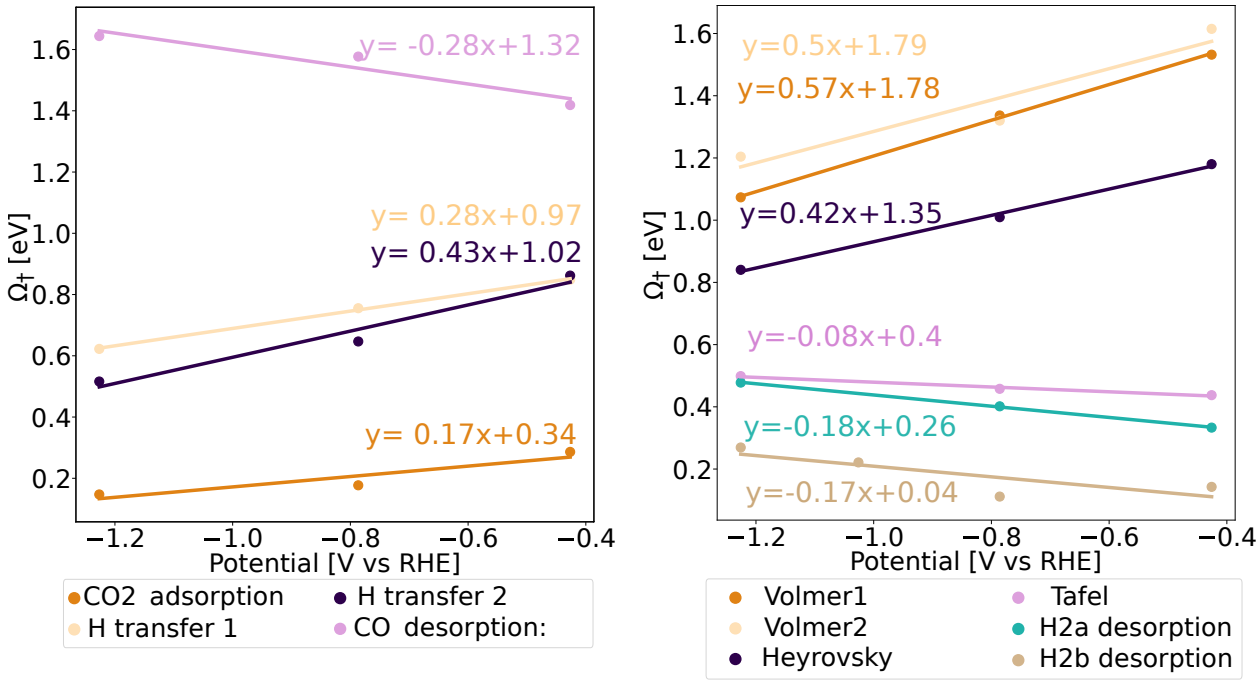

Figure 7: Forward grand free energy barrier, $\Omega_{\ddagger}$ as a function of potential. Linear fits for each CO2RR (left) and HER (right) step are given in the plots.

Volmer step is more than 1 eV larger than for the CO_2 adsorption at -0.8 V vs RHE and therefore CO_2 adsorption is kinetically preferred at the experimentally relevant potentials. The potential dependency is slightly smaller for the Heyrovsky step than for the second Volmer step, implying that at higher negative potentials a shift towards the Volmer-Tafel mechanism compared to the Volmer-Herovsky mechanism is expected.

Figure 8 displays the energy diagrams for the CO2RR and the HER at -0.8 V vs RHE, *i.e.* under the experimentally relevant CO2RR conditions. Comparison of the three reaction pathways shows that while the HER is thermodynamically favored over the CO2RR, the CO2RR is kinetically more facile: all CO2RR barriers to *CO are smaller than the first Volmer barrier. The more facile CO2RR kinetics at the $MoTe_2$ edge are the likely reason for the experimentally observed CO2RR activity in aqueous electrolytes.[25] These results emphasize the importance of computing reaction kinetics as a function of the electrode potential as the standard CHE approach including only thermodynamics would be unable to predict

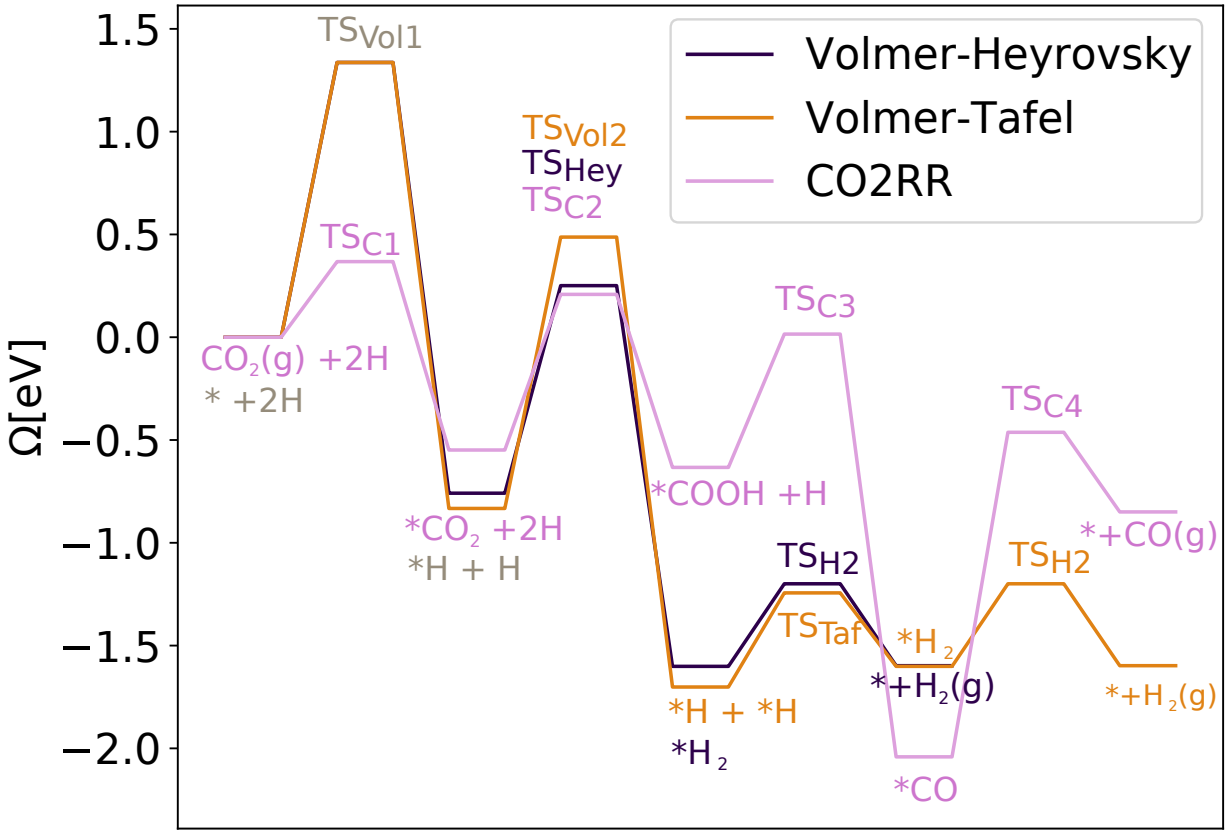

Figure 8: The Full grand free energy diagram for CO2RR and HER reaction pathways at -0.8 V vs RHE. (H^++e^-) is abbreviated "H". Grey text denotes energy levels that are the same for the Volmer-Heyrovsky and Volmer-Tafel mechanisms. TS denotes a transition state.

the preference for CO2RR over HER. It should be noted that the CHE approach also cannot describe the CO2RR selectivity of Ag, Au, and Cu metals.[68]

Conclusions

The reaction mechanisms of the CO_2 reduction reaction (CO2RR) and the competing Hydrogen Evolution Reaction (HER) at 2H-$MoTe_2$ edges were investigated employing a grand canonical ensemble DFT approach to explicitly include the electrode potential into calculations. We find that while HER is thermodynamically favored, the CO2RR is kinetically preferred over HER at the experimentally relevant potentials. This finding is in agreement with previous experimental results showing a relatively high CO2RR activity on $MoTe_2$ in an

aqueous electrolyte.[25] The potential dependency of energy barriers vary from one elementary step to the other. Interestingly, while the CO_2 adsorption barrier decreases for increasingly negative potentials, the reaction barrier for desorption of CO is increases, indicating that reduction beyond-CO could be enhanced at highly negative potentials. Furthermore, the first Volmer step depends more sensitively on the potential than CO2RR, so that the competing HER reaction will become relatively more important at high negative potentials. Overall, we find that the $MoTe_2$ edge is predicted to be an active and selective catalyst for alkaline CO2RR.

Acknowledgement

This project was funded by the Villum Foundation through the V-sustain project (No. 9455). Computational resources were provided by CSC IT Center for Science, Espoo, Finland. The authors furthermore thank Georg Kastlunger, Andreas Vishart, and Laura Laverdure for useful discussions.

Supporting Information Available

Atomic structures for the different water layers, Final and initial states for the NEB calculations, projected density of states plots, calculated capacitances and potentials of zero charge, number of excess electrons for the initial, transition and final states and a discussion about the imppact of the water layer size and configuration are available free of charge on the ACS Publications website.

References

(1) Garg, S.; Li, M.; Weber, A. Z.; Ge, L.; Li, L.; Rudolph, V.; Wang, G.; Rufford, T. E. Advances and challenges in electrochemical CO_2 reduction processes: An engineering

and design perspective looking beyond new catalyst materials. *Journal of Materials Chemistry A* **2020**, *8*, 1511–1544.

(2) Jordaan, S. M.; Wang, C. Electrocatalytic conversion of carbon dioxide for the Paris goals. *Nature Catalysis* **2021**, *4*, 915–920.

(3) Boutin, E.; Robert, M. Molecular Electrochemical Reduction of CO_2 beyond Two Electrons. *Trends in Chemistry* **2021**, *3*, 359–372.

(4) Su, D. J.; Xiang, S. Q.; Jiang, Y.; Liu, X.; Zhang, W.; Zhao, L. B. Binary alloys for electrocatalytic CO_2 conversion to hydrocarbons and alcohols. *Applied Surface Science* **2023**, *635*, 157734.

(5) Zhu, Y.; Yang, X.; Peng, C.; Priest, C.; Mei, Y.; Wu, G. Carbon-Supported Single Metal Site Catalysts for Electrochemical CO_2 Reduction to CO and Beyond. *Small* **2021**, *17*, 1–24.

(6) Hori, Y.; Murata, A.; Takahashi, R. Formation of hydrocarbons in the electrochemical reduction of carbon dioxide at a copper electrode in aqueous solution. *Journal of the Chemical Society, Faraday Transactions 1: Physical Chemistry in Condensed Phases* **1989**, *85*, 2309–2326.

(7) Nitopi, S.; Bertheussen, E.; Scott, S. B.; Liu, X.; Engstfeld, A. K.; Horch, S.; Seger, B.; Stephens, I. E.; Chan, K.; Hahn, C. et al. Progress and Perspectives of Electrochemical CO_2 Reduction on Copper in Aqueous Electrolyte. *Chemical Reviews* **2019**, *119*, 7610–7672.

(8) Woldu, A. R.; Huang, Z.; Zhao, P.; Hu, L.; Astruc, D. Electrochemical CO_2 reduction (CO_2 RR) to multi-carbon products over copper-based catalysts. *Coordination Chemistry Reviews* **2022**, *454*, 214340.

(9) Yu, J.; Wang, J.; Ma, Y.; Zhou, J.; Wang, Y.; Lu, P.; Yin, J.; Ye, R.; Zhu, Z.; Fan, Z. Recent Progresses in Electrochemical Carbon Dioxide Reduction on Copper-Based Catalysts toward Multicarbon Products. *Advanced Functional Materials* **2021**, *31*, 1–28.

(10) Li, H.; Shi, Y.; Chiu, M. H.; Li, L. J. Emerging energy applications of two-dimensional layered transition metal dichalcogenides. *Nano Energy* **2015**, *18*, 293–305.

(11) Cha, E.; Kim, D. K.; Choi, W. Advances of 2D MoS_2 for High-Energy Lithium Metal Batteries. *Frontiers in Energy Research* **2021**, *9*, 1–7.

(12) Krishnan, U.; Kaur, M.; Singh, K.; Kumar, M.; Kumar, A. A synoptic review of MoS_2 : Synthesis to applications. *Superlattices and Microstructures* **2019**, *128*, 274–297.

(13) Yang, E.; Ji, H.; Jung, Y. Two-Dimensional Transition Metal Dichalcogenide Monolayers as Promising Sodium Ion Battery Anodes. *Journal of Physical Chemistry C* **2015**, *119*, 26374–26380.

(14) Zhang, G.; Liu, H.; Qu, J.; Li, J. Two-dimensional layered MoS_2: Rational design, properties and electrochemical applications. *Energy and Environmental Science* **2016**, *9*, 1190–1209.

(15) Cao, Y. Roadmap and Direction toward High-Performance MoS_2 Hydrogen Evolution Catalysts. *ACS Nano* **2021**, *15*, 11014–11039.

(16) Feng, C.; Ma, J.; Li, H.; Zeng, R.; Guo, Z.; Liu, H. Synthesis of molybdenum disulfide (MoS_2) for lithium ion battery applications. *Materials Research Bulletin* **2009**, *44*, 1811–1815.

(17) Xie, X.; Ao, Z.; Su, D.; Zhang, J.; Wang, G. MoS_2/graphene composite anodes with enhanced performance for sodium-ion batteries: The role of the two-dimensional heterointerface. *Advanced Functional Materials* **2015**, *25*, 1393–1403.

(18) Asadi, M.; Kim, K.; Liu, C.; Addepalli, A. V.; Abbasi, P.; Yasaei, P.; Phillips, P.; Behranginia, A.; Cerrato, J. M.; Haasch, R. et al. Nanostructured transition metal dichalcogenide electrocatalysts for CO_2 reduction in ionic liquid. *Science* **2016**, *353*, 467–470.

(19) Abbasi, P.; Asadi, M.; Liu, C.; Sharifi-Asl, S.; Sayahpour, B.; Behranginia, A.; Zapol, P.; Shahbazian-Yassar, R.; Curtiss, L. A.; Salehi-Khojin, A. Tailoring the Edge Structure of Molybdenum Disulfide toward Electrocatalytic Reduction of Carbon Dioxide. *ACS Nano* **2017**, *11*, 453–460.

(20) Brea, C.; Hu, G. Shifting and breaking scaling relations at transition metal telluride edges for selective electrochemical CO_2 reduction. *Journal of Materials Chemistry A* **2022**, *10*, 10162–10170.

(21) Qorbani, M.; Sabbah, A.; Lai, Y. R.; Kholimatussadiah, S.; Quadir, S.; Huang, C. Y.; Shown, I.; Huang, Y. F.; Hayashi, M.; Chen, K. H. et al. Atomistic insights into highly active reconstructed edges of monolayer 2H-WSe_2 photocatalyst. *Nature Communications* **2022**, *13*, 1–8.

(22) Giuffredi, G.; Asset, T.; Liu, Y.; Atanassov, P.; Di Fonzo, F. Transition Metal Chalcogenides as a Versatile and Tunable Platform for Catalytic CO_2 and N_2 Electroreduction. *ACS Materials Au* **2021**, *1*, 6–36.

(23) Pedersen, P. D.; Vegge, T.; Bligaard, T.; Hansen, H. A. Trends in CO_2 Reduction on Transition Metal Dichalcogenide Edges. *ACS Catalysis* **2023**, *13*, 2341–2350.

(24) Bagger, A.; Ju, W.; Varela, A. S.; Strasser, P.; Rossmeisl, J. Electrochemical CO_2 Reduction: A Classification Problem. *ChemPhysChem* **2017**, *18*, 3266–3273.

(25) Liu, X.; Yang, H.; He, J.; Liu, H.; Song, L.; Li, L.; Luo, J. Highly Active, Durable Ultrathin $MoTe_2$ Layers for the Electroreduction of CO_2 to CH_4. *Small* **2018**, *14*, 1–7.

(26) Lauritsen, J. V.; Nyberg, M.; Vang, R. T.; Bollinger, M. V.; Clausen, B. S.; Topsøe, H.; Jacobsen, K. W.; Lægsgaard, E.; Nørskov, J. K.; Besenbacher, F. Chemistry of one-dimensional metallic edge states in MoS_2 nanoclusters. *Nanotechnology* **2003**, *14*, 385–389.

(27) Bollinger, M. V.; Lauritsen, J. V.; Jacobsen, K. W.; Nørskov, J. K.; Helveg, S.; Besenbacher, F. One-dimensional metallic edge states in MoS_2. *Physical Review Letters* **2001**, *87*, 3–6.

(28) Voiry, D.; Salehi, M.; Silva, R.; Fujita, T.; Chen, M.; Asefa, T.; Shenoy, V. B.; Eda, G.; Chhowalla, M. Conducting MoS_2 nanosheets as catalysts for hydrogen evolution reaction. *Nano Letters* **2013**, *13*, 6222–6227.

(29) Wang, J.; Liu, J.; Zhang, B.; Ji, X.; Xu, K.; Chen, C.; Miao, L.; Jiang, J. The mechanism of hydrogen adsorption on transition metal dichalcogenides as hydrogen evolution reaction catalyst. *Physical Chemistry Chemical Physics* **2017**, *19*, 10125–10132.

(30) Chung, D. Y.; Park, S. K.; Chung, Y. H.; Yu, S. H.; Lim, D. H.; Jung, N.; Ham, H. C.; Park, H. Y.; Piao, Y.; Yoo, S. J. et al. Edge-exposed MoS_2 nano-assembled structures as efficient electrocatalysts for hydrogen evolution reaction. *Nanoscale* **2014**, *6*, 2131–2136.

(31) Lin, L.; Feng, Z.; Dong, Z.; Hu, C.; Han, L.; Tao, H. DFT study on the adsorption of CO, NO_2, SO_2 and NH_3 by Te vacancy and metal atom doped $MoTe_2$ monolayers. *Physica E: Low-Dimensional Systems and Nanostructures* **2023**, *145*, 115489.

(32) Szary, M. J.; Babelek, J. A.; Florjan, D. M. Dopant-sheet interaction and its role in the enhanced chemical activity of doped $MoTe_2$. *Surface Science* **2022**, *723*, 122093.

(33) Hossain, M. D.; Liu, Z.; Liu, H.; Tyagi, A.; Rehman, F.; Li, J.; Amjadian, M.; Cai, Y.; Goddard, W. A.; Luo, Z. The kinetics and potential dependence of the hydrogen evolution reaction optimized for the basal-plane Te vacancy site of $MoTe_2$. **2023**, *3*, 100489.

(34) Jinnouchi, R.; Kodama, K.; Morimoto, Y. Electronic structure calculations on electrolyte–electrode interfaces: Successes and limitations. *Current Opinion in Electrochemistry* **2018**, *8*, 103–109.

(35) Sakaushi, K.; Kumeda, T.; Hammes-Schiffer, S.; Melander, M. M.; Sugino, O. Advances and challenges for experiment and theory for multi-electron multi-proton transfer at electrified solid–liquid interfaces. *Phys. Chem. Chem. Phys.* **2020**, *22*, 19401–19442.

(36) Yang, X.; Bhowmik, A.; Vegge, T.; Hansen, H. A. Neural Network Potentials for Accelerated Metadynamics of Oxygen Reduction Kinetics at Au-Water Interfaces. *Chemical Science* **2023**, 3913–3922.

(37) Qin, X.; Vegge, T.; Hansen, H. A. Cation-Coordinated Inner-Sphere CO_2 Electroreduction at Au-Water Interfaces. *Journal of the American Chemical Society* **2023**, *145*, 1897–1905.

(38) Melander, M. M. Grand canonical ensemble approach to electrochemical thermodynamics, kinetics, and model Hamiltonians. *Current Opinion in Electrochemistry* **2021**, *29*, 100749.

(39) Nørskov, J. K.; Rossmeisl, J.; Logadottir, A.; Lindqvist, L.; Kitchin, J. R.; Bligaard, T.; Jónsson, H. Origin of the overpotential for oxygen reduction at a fuel-cell cathode. *Journal of Physical Chemistry B* **2004**, *108*, 17886–17892.

(40) Melander, M. M.; Kuisma, M. J.; Christensen, T. E. K.; Honkala, K. Grand-canonical approach to density functional theory of electrocatalytic systems: Thermodynamics of solid-liquid interfaces at constant ion and electrode potentials. *Journal of Chemical Physics* **2019**, *150*, 041706.

(41) Wu, T.; Melander, M. M.; Honkala, K. Coadsorption of NRR and HER Intermediates Determines the Performance of Ru-N4 toward Electrocatalytic N_2 Reduction. *ACS Catalysis* **2022**, *12*, 2505–2512.

(42) Verma, A. M.; Laverdure, L.; Melander, M. M.; Honkala, K. Mechanistic Origins of the pH Dependency in Au-Catalyzed Glycerol Electro-oxidation: Insight from First-Principles Calculations. *ACS Catalysis* **2022**, *12*, 662–675.

(43) Abidi, N.; Bonduelle-Skrzypczak, A.; Steinmann, S. N. Revisiting the Active Sites at the MoS_2/H_2O Interface via Grand-Canonical DFT: The Role of Water Dissociation. *ACS Applied Materials and Interfaces* **2020**, *12*, 31401–31410.

(44) Goodpaster, J. D.; Bell, A. T.; Head-Gordon, M. Identification of Possible Pathways for C-C Bond Formation during Electrochemical Reduction of CO_2 : New Theoretical Insights from an Improved Electrochemical Model. *Journal of Physical Chemistry Letters* **2016**, *7*, 1471–1477.

(45) Singh, M. R.; Goodpaster, J. D.; Weber, A. Z.; Head-Gordon, M.; Bell, A. T. Mechanistic insights into electrochemical reduction of CO_2 over Ag using density functional theory and transport models. *Proceedings of the National Academy of Sciences of the United States of America* **2017**, *114*, E8812–E8821.

(46) Zhang, H.; Goddard, W. A.; Lu, Q.; Cheng, M. J. The importance of grand-canonical quantum mechanical methods to describe the effect of electrode potential on the stability of intermediates involved in both electrochemical CO_2 reduction and hydrogen evolution. *Physical chemistry chemical physics : PCCP* **2018**, *20*, 2549–2557.

(47) Kastlunger, G.; Wang, L.; Govindarajan, N.; Heenen, H. H.; Ringe, S.; Jaramillo, T.; Hahn, C.; Chan, K. Using pH Dependence to Understand Mechanisms in Electrochemical CO Reduction. *ACS Catalysis* **2022**, *12*, 4344–4357.

(48) Enkovaara, J.; Rostgaard, C.; Mortensen, J. J.; Chen, J.; Dułak, M.; Ferrighi, L.; Gavnholt, J.; Glinsvad, C.; Haikola, V.; Hansen, H. A. et al. Electronic structure calculations with GPAW: A real-space implementation of the projector augmented-wave method. *Journal of Physics Condensed Matter* **2010**, *22*, 253202.

(49) Mortensen, J. J.; Hansen, L. B.; Jacobsen, K. W. Real-space grid implementation of the projector augmented wave method. *Physical Review B - Condensed Matter and Materials Physics* **2005**, *71*, 1–11.

(50) Larsen, A. H.; Mortensen, J. J.; Blomqvist, J.; Castelli, I. E.; Christensen, R.; Dułak, M.; Friis, J.; Groves, M. N.; Hammer, B.; Hargus, C. et al. The atomic simulation environment—a Python library for working with atoms. *Journal of Physics: Condensed Matter* **2017**, *29*, 273002.

(51) Wellendorff, J.; Lundgaard, K. T.; Møgelhøj, A.; Petzold, V.; Landis, D. D.; Nørskov, J. K.; Bligaard, T.; Jacobsen, K. W. Density functionals for surface science: Exchange-correlation model development with Bayesian error estimation. *Phys. Rev. B* **2012**, *85*, 235149.

(52) Kastlunger, G.; Lindgren, P.; Peterson, A. A. Controlled-Potential Simulation of Elementary Electrochemical Reactions: Proton Discharge on Metal Surfaces. *Journal of Physical Chemistry C* **2018**, *122*, 12771–12781.

(53) Held, A.; Walter, M. Simplified continuum solvent model with a smooth cavity based on volumetric data. *Journal of Chemical Physics* **2014**, *141*, 174108.

(54) Batsanov, S. S. Van der Waals radii of elements. *Inorganic Materials* **2001**, *37*, 871–885.

(55) Peterson, A. A. Global optimization of adsorbate-surface structures while preserving molecular identity. *Topics in Catalysis* **2014**, *57*, 40–53.

(56) Trasatti, S. The absolute electrode potential: An explanatory note. *J. Electroanal. Chem.* **1986**, *209*, 417–428.

(57) Jónsson, H.; Mills, G.; Jacobsen, K. W. Nudged elastic band method for finding minimum energy paths of transitions. **1998**, 385–404.

(58) Henkelman, G.; Jónsson, H. Improved tangent estimate in the nudged elastic band method for finding minimum energy paths and saddle points. *Journal of Chemical Physics* **2000**, *113*, 9978–9985.

(59) Henkelman, G.; Jónsson, H. A climbing image nudged elastic band method for finding saddle points and minimum energy paths and minimum energy paths. *Journal of chemical Physics* **2000**, *113*, 9901–9904.

(60) Bader, R. *Atoms in Molecules: A Quantum Theory*; International Ser. of Monogr. on Chem; Clarendon Press, 1994.

(61) Tang, W.; Sanville, E.; Henkelman, G. A grid-based Bader analysis algorithm without lattice bias. *Journal of Physics Condensed Matter* **2009**, *21*, 084204.

(62) Henkelman, G.; Arnaldsson, A.; Jónsson, H. A fast and robust algorithm for Bader decomposition of charge density. *Computational Materials Science* **2006**, *36*, 354–360.

(63) Yu, M.; Trinkle, D. R. Accurate and efficient algorithm for Bader charge integration. *Journal of Chemical Physics* **2011**, *134*, 1–8.

(64) Dong, J.; Ding, D.; Jin, C.; Liu, Y.; Ding, F. Edge Reconstruction-Dependent Growth Kinetics of MoS_2. *ACS Nano* **2023**, *17*, 127–136.

(65) Duan, Z.; Henkelman, G. Theoretical Resolution of the Exceptional Oxygen Reduction Activity of Au(100) in Alkaline Media. *ACS Catalysis* **2019**, *9*, 5567–5573.

(66) Domínguez-Flores, F.; Melander, M. M. Approximating constant potential DFT with canonical DFT and electrostatic corrections. *The Journal of Chemical Physics* **2023**, *158*, 144701.

(67) Melander, M. M. Grand Canonical Rate Theory for Electrochemical and Electrocatalytic Systems I: General Formulation and Proton-coupled Electron Transfer Reactions. *Journal of The Electrochemical Society* **2020**, *167*, 116518.

(68) Shi, C.; Hansen, H. A.; Lausche, A. C.; Nørskov, J. K. Trends in electrochemical CO_2 reduction activity for open and close-packed metal surfaces. *Physical Chemistry Chemical Physics* **2014**, *16*, 4720–4727.

TOC Graphic